JGR Space Physics

Key Points:
- Hardening/softening of the aurora electron spectrum during a pulsating aurora event was estimated from camera and riometer measurements
- In the lower-latitude aurora, spectrum hardening and softening coexisted separating into oscillation periods shorter and longer than 40 s

Correspondence to:
S.-I. Oyama,
soyama@isee.nagoya-u.ac.jp

Variations in Cosmic Noise Absorption in Association With Equatorward Development of the Pulsating Auroral Patch: A Case Study to Estimate the Energy Spectra of Auroral Precipitating Electrons

Taishiro Miyamoto[1,2], Shin-ichiro Oyama[1,3] , Tero Raita[4] , Keisuke Hosokawa[5] , Yoshizumi Miyoshi[1] , Yasunobu Ogawa[3] , and Satoshi Kurita[6]

[1]Institute for Space-Earth Environmental Research, Nagoya University, Nagoya, Japan, [2]Now at Nippon Steel Corporation Nagoya Works, Tokai-shi, Japan, [3]National Institute of Polar Research, Tokyo, Japan, [4]Sodankylä Geophysical Observatory, University of Oulu, Oulu, Finland, [5]Center for Space Science and Radio Engineering, University of Electro-Communications, Chōfu, Japan, [6]Research Institute for Sustainable Humanosphere, Kyoto University, Kyoto, Japan

Abstract This study focused on a pulsating aurora event associated with aurora morphological changes in Fennoscandia in the early morning on March 7, 2017. A high-speed sampling all-sky camera captured equatorward development of the pulsating auroral patch in association with a substorm centered over the Greenland/North America region. Of particular interest in this event is the interconnection between the auroral intensity and the cosmic noise absorption (CNA) derived from three riometers aligned meridionally in Finland (from north to south: Ivalo, Sodankylä, and Rovaniemi). The analysis was made by dividing optical measurements into two oscillation components: longer and shorter than 40 s, that is, nonpulsating and pulsating auroral modulations. The interrelation between the auroral brightness and CNA showed a linear correlation. The inclination of the regression line changed with time depending on latitudes, which was interpreted as hardening or softening of the precipitating electron spectrum. Especially in the case of the low-pass component, the inclination of the CNA-vs-intensity interrelation increased at the three riometer latitudes in the substorm recovery phase. On the other hand, for the high-pass component, the inclination decreased at Rovaniemi (lower latitude) but remained uniform at Sodankylä (higher latitude). These features suggest that the precipitating electron spectrum has softened in the low-pass or nonpulsating auroral component, but the spectrum has hardened in the high-pass or pulsating auroral component on the lower latitude part of the auroral patch region. This study proposes a new application of riometer-camera measurements to examine auroral particle precipitation.

1. Introduction

A pulsating aurora is characterized by quasiperiodic modulations in emission intensity at the second order of the main pulsation and subsecond order of the internal modulations. Based on the particle excitation and successive radiation process, auroral electron precipitation also takes place at these periodicities during a pulsating aurora. To find experimental evidence of the periodic precipitation mechanism, conjugate observations have recently been obtained with ground-based cameras and magnetospheric satellites. For example, Hosokawa et al. (2020) presented an excellent agreement between emission intensity pulsations and time variations in the chorus wave regarding both the main pulsation and the internal modulation of the pulsating aurora. Ozaki et al. (2019) succeeded in visualizing the chorus wave and plasma particle interactions in the magnetosphere during an auroral flash event. These results strongly support the theoretical prediction of the relationship between magnetospheric electrons and chorus waves (Ni et al., 2011; Thorne et al., 2010). The theoretical study also predicted energetic electron precipitation mostly exceeding approximately 10 keV during a pulsating aurora. Periodic electron precipitation above a few keV and the coinciding pulsating aurora were directly measured with cameras and the particle sensor onboard the Reimei satellite (Miyoshi, Saito, et al., 2015). More energetic electron precipitations at the MeV class can be occurred during the pulsating aurora, which are predicted by an observation-driven simulation (Miyoshi, Oyama, et al., 2015), although its demonstration by conjugate measurements with magnetospheric satellites and ground-based cameras has not been achieved yet.

Precipitating electrons at energies higher than 10 keV ionize neutral particles below 100–110 km (Turunen et al., 2009). The ionospheric responses during the pulsating aurora have been studied by analyzing measurements with various radio-wave techniques. In particular, the incoherent scatter radar (ISR) is the most powerful diagnostic tool to derive the height-resolved electron density, which can be used for estimating the energy of the precipitating electron. Hosokawa and Ogawa (2015) compared two height profiles of the electron density taken during pulsating aurora ON and OFF intervals and presented a density increase at 100–110 km altitude for the ON phase. These researchers also performed a statistical analysis of the E-region peak height, which suggested descent at 6–9 magnetic local time (MLT). Partamies et al. (2017) presented the descent of the auroral emission height in the morning based on a statistical analysis of pulsating aurora images. While these statistical results may give an impression that the ionization and auroral heights successively decrease for the morning sector, development can be more sporadic for individual events coinciding with substorm activity that occurred at midnight. Oyama et al. (2017) studied an event that included three substorms at night and showed that the lowest height of ionization decreased every substorm, finally reaching 65 km for the third substorm, which occurred in the late morning. An inversion method was applied to the height-resolved electron density to estimate the precipitating electron energy spectrum, and the spectra at individual substorms revealed a flux increase at energies higher than 10 keV, which is known as "hardening." At the second substorm, which occurred at 4.5 MLT, the spectrum hardening coincided with equatorward excursion of the pulsating aurora in association with its fragmentation. Auroral fragmentation into patches is a common feature in the postmidnight period (Hashimoto et al., 2015; Shiokawa et al., 2014). Then, a scientific question to be conceived from the previous results of spectrum hardening and auroral fragmentation is "Does spectrum hardening at the postmidnight time associate with morphological changes in the pulsating aurora?" This question is the scientific motivation of this study.

A riometer is a passive radio wave receiver sensitive to ionization in the D-region ionosphere, and riometers measure HF radio absorption or cosmic noise absorption (CNA) at heights where the electron motion is partially dominated by collisions with neutral particles. The HF radio frequency widely adopted for the riometer is in the 30 MHz range, which has a sensitivity peak at approximately 90 km (Hargreaves, 1995; Tanaka et al., 2007). CNA has been compared with auroral brightness for more than half a century (e.g., Arnoldy et al., 1982; Brekke, 1971; Campbell & Leinbach, 1961), and the general results have shown good agreement between the two temporal variations. The result is physically acceptable according to the ionization and excitation processes associated with auroral electron precipitation. An important point we should focus on is the altitudinal discrepancy between the sensitivity peak of the riometer and auroral emission height because it may advert the evolution of the precipitating electron energy. Since the auroral emission height is mostly higher than the riometer sensitivity peak at 90 km, the precipitating electron energy responsible for the aurora brightness is lower than that for CNA. A theoretical calculation of the ionization rate suggests that monoenergetic electron precipitation at an energy of 40 keV has an ionization peak at 90 km (Turunen et al., 2009).

Remarkable experimental evidence was recently reported from CNA-aurora comparison studies. McKay et al. (2018) analyzed a zonally elongated auroral arc at the substorm growth phase and found a CNA arc parallel to the optical emission arc but displaced to its equator side. Since pulsating aurorae were embedded in the CNA enhanced region or equator side of the growth-phase arc during the event, D-region density enhancement associated with energetic electron precipitation is likely causal of CNA production. On the other hand, notable E-region electron-temperature enhancements induced by the Farley-Buneman instability in association with a large electric field near the growth-phase arc may also cause CNA (D'Angelo, 1976; Jussila et al., 2004; Stauning, 1984). Grandin et al. (2017) presented good correlations between the time series of the CNA and the main modulation of the pulsating aurora. These correlations are evidence that the precipitating electron flux at the energy responsible for pulsating aurora brightness (approximately 10 keV) may vary synchronously with that at the energy responsible for CNA (approximately 40 keV). A similar correlation of the pulsating aurora electron flux was found in the rocket measurement (Sandahl et al., 1980). A comparison of the CNA and pulsating aurora has also been made by focusing on the auroral morphology. Yang et al. (2019) performed a statistical analysis of CNA and aurora brightness obtained from a single-beam riometer and an all-sky camera collocated in Gillam, Canada, grouping pulsating aurora measurements into two patch structures: patchy pulsating aurora (PPA) and amorphous pulsating aurora (APA) (Grono & Donovan, 2018). Their results showed that the CNA is systematically higher in APA than
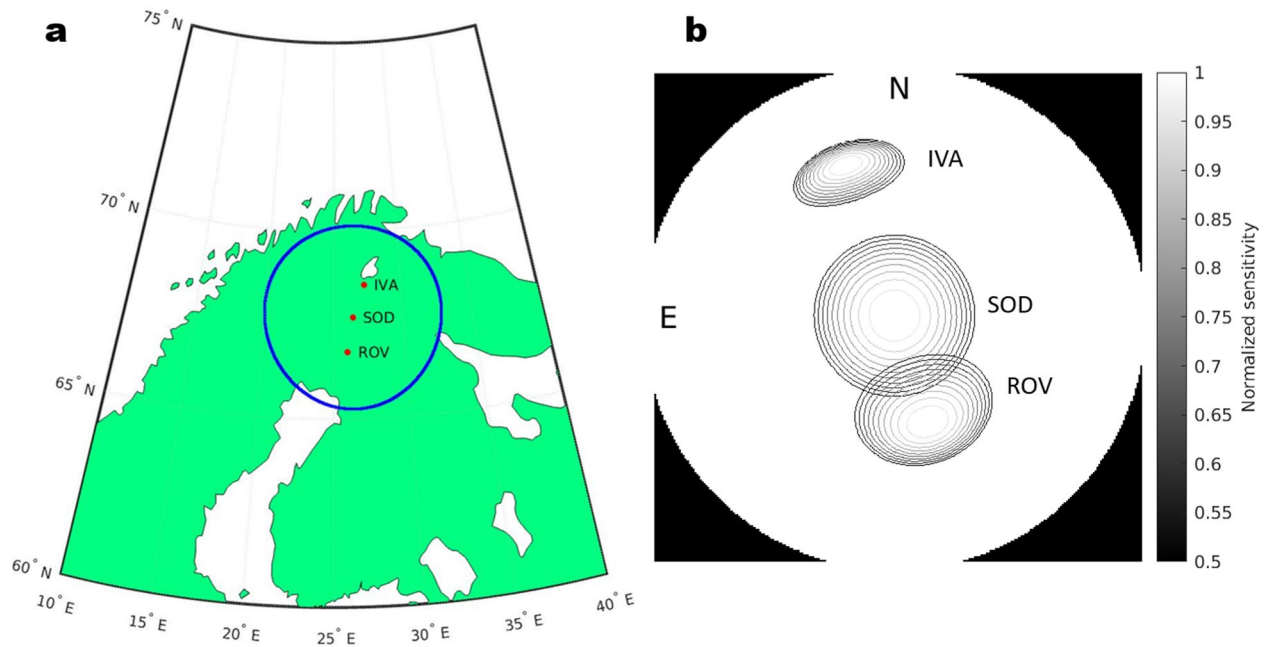
Figure 1. (a) Map presents the location of the riometers adopted in this study (red dots; IVA: Ivalo, SOD: Sodankylä, ROV: Rovaniemi) and the field of view of the electron multiplying charge-coupled device camera at SOD. (b) Horizontal patterns of the riometer sensitivity normalized by values at individual zenith points, which are mapped on the all-sky camera image taken from SOD. Note that top is north and left is east.

in PPA, and the flatter slope of the CNA-brightness distribution for APA suggested harder electron precipitation than that for PPA (see Figure 3b in Yang et al., 2019). However, this feature might be an argument regarding the temporal evolution of precipitating spectrum hardening in the morning sector (Hosokawa & Ogawa, 2015; Oyama et al., 2017) and patch formation characterized by auroral fragmentation (Hashimoto et al., 2015; Shiokawa et al., 2014). It is possible that latitudinal dependencies of the PPA appearance and auroral fragmentation relative to the main auroral oval are subject to appear at the equatorward side of the oval. Other statistical analysis of the ionospheric density presents that density enhancements below 100 km are more significant during PPA than those during APA, which suggests that the precipitating electron energy during PPA tends to be higher than that during APA (Tesema et al., 2020). Therefore, it is important to study the temporal evolution and spatial distribution of the precipitating electron energy and the auroral morphology.

This study focuses on a pulsating auroral event, including equatorward excursion of the patches coinciding with a substorm onset, that occurred in the Greenland/North American area. We analyzed CNA measured from the meridional riometer chain in Finland along with auroral images that overlapped the field-of-views of the riometers. This data set is unique for studying the time evolution and spatial distribution of the pulsating aurora and the latitudinal dependence of the precipitating electron energy.

2. Observation Data and Analysis Methods

2.1. Electron Multiplying Charge-Coupled Device (EMCCD) Camera and Riometer

In this study, we used an electron multiplying charge-coupled device (EMCCD) all-sky camera in Sodankylä (geographic: 67.4°N, 26.4°E; SOD) and three riometers in Ivalo (geographic: 68.6°N, 27.3°E; IVA), Sodankylä and Rovaniemi (geographic: 66.8°N, 26.0°E; ROV) in Finland. Figure 1a shows a map of Fennoscandia pointing to the three riometer stations (red dots) and the camera field of view (FOV) which is drawn assuming a height of 100 km and zenith angle of 70°.

An optical filter (RG665) was mounted on the EMCCD camera to cut light at wavelengths shorter than 665 nm. The EMCCD camera mainly measured the N_2 first positive (1PG) emissions, which are known as prompt emissions, and the typical emission height profile peaks at approximately 100 km. The original time

resolution is 0.01 s, but to improve the signal-to-noise ratio, ten camera images have been averaged in this study, resulting in a time resolution of 0.1 s, which is adequate for finding pulsating aurora. More detailed information on the camera system can be found in Hosokawa et al. (2020).

Wide beam (60°) riometers, which have been operated at 30 MHz at IVA and SOD and 32.4 MHz at ROV, theoretically have the highest sensitivity at an altitude of approximately 90 km (Hargreaves, 1995; Tanaka et al., 2007). Since the ionization rate for a monoenergetic beam of electrons at 40 keV has a peak at 90 km (Turunen et al., 2009), temporal variations in the CNA derived from the riometer represent those in the precipitating electron flux at approximately 40 keV. The scientific objective of this study is to examine the evolution of the precipitating electron energy in response to the spatial development of the pulsating aurora, with a particular focus on latitudinal distributions. This motivation is unique and different from previous studies in this field, which focused on CNA modulations with the pulsating aurora (Brekke, 1971; Campbell & Leinbach, 1961; Grandin et al., 2017). While the original sampling time of the riometer is 0.1 s, a 60-s mean CNA was analyzed in this study. Sensitivity of the three riometers is not identical, which means that the CNA value derived from each riometer may be different even if the ionospheric density is identical. Therefore, this study will not compare the CNA values itself between the three sites.

2.2. Mapping the Riometer FOV on the Camera Image

The riometer beam pattern has a maximum sensitivity in the zenith decreasing isotropically according to a parabolic function of the zenith angle. In this study, the beam width at half of the maximum is defined as 60°, and the sensitivity at the edge of the FOV (outer black circle of each FOV in Figure 1b) becomes half of that at the zenith. Figure 1b shows the horizontal pattern of the sensitivity normalized by the zenith value and mapped on the EMCCD camera image frame taken at Sodankylä assuming the sensitivity peak at 90 km. Three patterns at IVA, SOD, and ROV are illustrated in gray-scale contours. In the analytical procedure used to calculate the mean optical count, to equalize the measurement area with the riometers and the EMCCD camera, the normalized sensitivity pattern was multiplied by the camera count as individual weighting functions. This method was also adopted by Grandin et al. (2017). Calculation in this study assumes the auroral emission height of 100 km as mentioned in Section 2.1. The assumed height hardly affects results derived from measurements in Sodankylä and Rovaniemi because these riometer FOVs are near the center of the camera FOV, but it may occur in results for Ivalo. However, the emission height of 100 km is adopted through the calculation in this study because it is consistent with a statistical result of the emission height at postmidnight (Partamies et al., 2017).

2.3. Theoretical Approach to the Relationship Between Aurora Emission Intensity and CNA

In the E region, the number density of molecular ions is 10 times or more than that of atomic ions. Due to the recombination process for the molecular ions that is considerably faster than for the atomic ions, by two orders or more, and negligibly small contributions of the plasma diffusion to the ionization process, the loss rate (L), which may be equivalent to the recombination rate in a steady state, can be proportional to the molecular ion density times the electron density (N_e) or approximately square of the electron density. Then, the production rate (Q) can be written as

$$Q = L = \alpha_{\text{eff}} N_e^2, \tag{1}$$

where α_{eff} is the effective recombination coefficient (Vickrey et al., 1982). Since the excitation rate of the neutral particles associated with auroral electron precipitation is statistically proportional to Q, the aurora emission intensity (I) is proportional to Q (Oyama et al., 2013 and references therein). Then, the auroral emission intensity (I) can be related to the electron density, as shown in Equation 2.

$$\sqrt{I} \propto \sqrt{\alpha_{\text{eff}}} N_e \tag{2}$$

The CNA in dB can be calculated as a function of electron density and electron-neutral collision frequency (Oyama et al., 2017).

$$\text{CNA} = 4.6 \times 10^{-5} \int_{65\text{km}}^{120\text{km}} \frac{N_e(h)\nu_{en}(h)}{\omega^2 + \nu_{en}^2(h)} dh, \tag{3}$$

Equation 3 suggests that CNA can correlate with the electron density, and by comparing with Equation 2, the square root of the emission intensity may be approximately proportional to CNA.

$$\sqrt{I} \propto \text{CNA} \tag{4}$$

Note that the unit of CNA in Equations 3 and 4 is dB. In the derivation of Equation 4, fluctuations in α_{eff} are ignored despite their dependencies on the background ionospheric condition, for instance, the electron temperature (Torr et al., 1976). According to previous results summarized by Vickrey et al. (1982), the effective recombination coefficient at an altitude of 100 km can be varied by a factor of two, but the electron density in the E and D regions can be varied by 1–2 orders of magnitude during auroral precipitation. Thus, the ambiguity of α_{eff} can be ignored in this study.

3. Results

3.1. Event Conditions

Figure 2 shows temporal variations in (a) solar wind speed, (b) proton density, (c–d) interplanetary magnetic field (IMF) Bz and By components (in GSM coordinates), (e) SYM-H and (f) AL index for seven days from March 1, 2017. The proton density was enhanced, and the IMF fluctuated on March 1 before the arrival of high-speed solar wind, which is a typical signature of the corotating interaction region (CIR) (Kataoka & Miyoshi, 2006). SYM-H shows that the development of the storm coincides with the CIR and the successive recovery phase. The AL index presents many sharp drops in the magnetic field as an indication of a substorm, and shows continuous activities during the recovery phase. The vertical bars in magenta are marked at 2–3 UT on March 7, 2017, which is the period of focus in this study. Based on these measurements, it is considered that the event occurred in a substorm during the storm recovery phase associated with CIR following high-speed coronal hole stream. During the recovery phase of the CIR storm, continuous hot electron injections and chorus wave enhancements are commonly seen in the magnetosphere (Miyoshi et al., 2013).

The AL index is also presented in Figure 3 but closely looks at a time period around the event, which is hatched in magenta, along with magnetometer measurements at nine AL stations. At 20 UT, the AL index peaked negative, reaching approximately −1,000 nT. Corresponding negative deviations were recorded at DIK and TIK in Russia. Measurements at ABK (Sweden) also suggest the development of substorm activity, but the main region of the substorm is estimated in Siberia rather than Scandinavia. At approximately 22–23 UT, the AL index indicates a subsequent substorm with corresponding development at ABK, LRV (Iceland) and DIK. The principal substorm location drifted westward from Siberia to Scandinavia for 2–3 h. From 23 to 0 UT, the AL index presents an aspect of the substorm recovery phase. After 1 UT, a negative bay of AL has been developed again. While the substorm onset time is obscure because of repeated development of the negative bay, a peak reached the minimum value at 02:42 UT in association with enhancements at LRV and NAQ along with a subordinate peak at ABK. NAQ and LRV met negative peaks periodically after 3 UT, but the development at ABK seemed to have abated. The current peak tends to be located at approximately magnetic local midnight, and the westward drift of the current peak location is caused by the Earth's rotation. The interval of focus in this study is the third substorm of the night.

Figures 4a and 4b show two snapshots of the all-sky image taken at Sodankylä as representative aurorae that appeared at 2:00–2:40 UT (T1) and 2:40–3:00 UT (T2), respectively, along with contour plots of the riometer sensitivity at the three sites. The top and left sides of the image are north (N) and east (E), respectively. For T1, the sky was characterized by smaller and weaker pulsating patches mainly in the northern half of the FOV. However, for T2, several brighter and larger patches appeared in the wide area of the FOV. Figure 4c presents a meridional keogram made of the camera images. A yellow rectangle presents the time interval highlighted in this study. Equatorward of the long-lasting bright aurora remaining at higher latitudes (near IVA), pulsating auroral patches emerged and expanded equatorward (faint gray stripes in the keogram). The first detectable patches may have been seen at 2:10 UT between IVA and SOD, which can also be identified
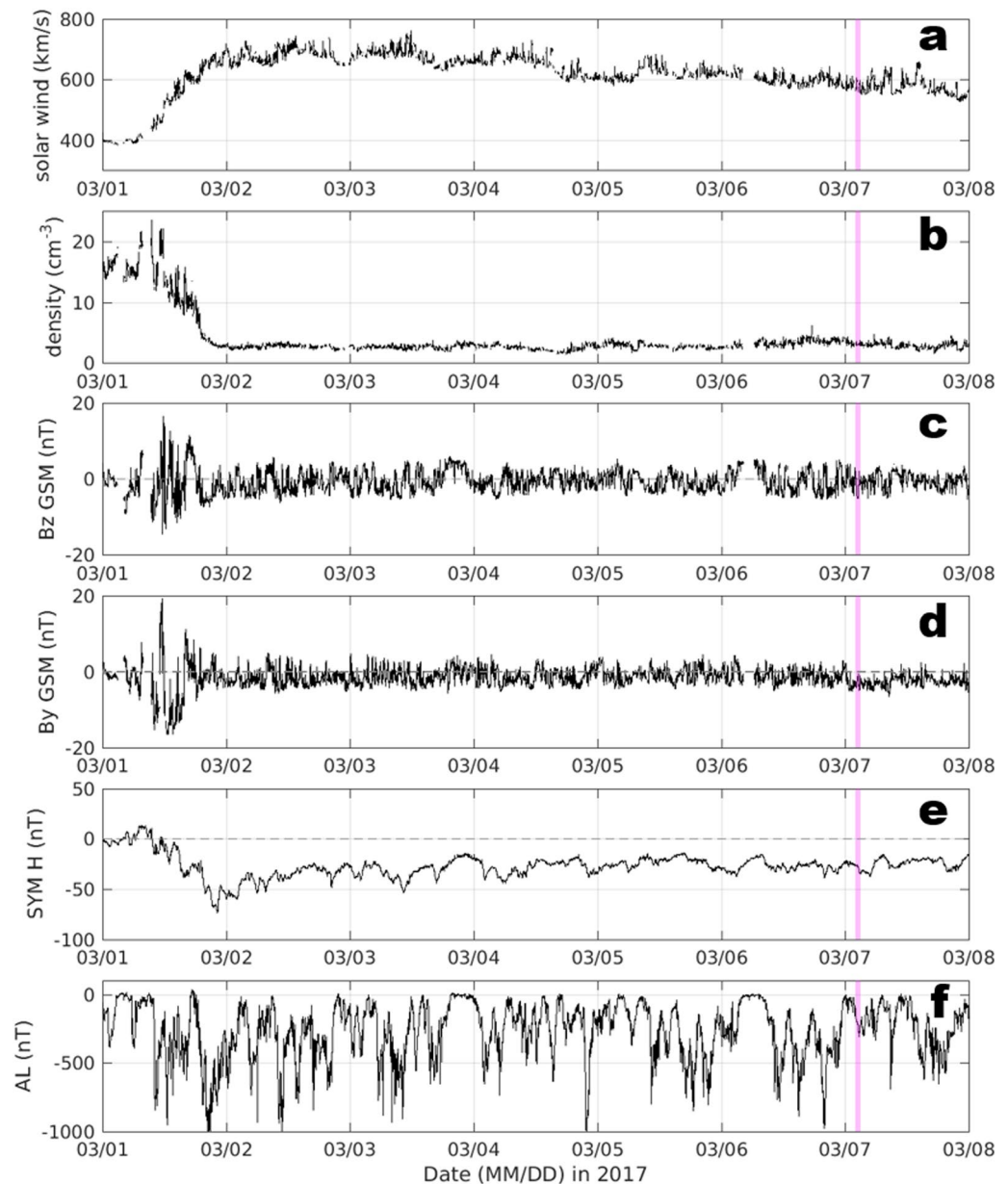
Figure 2. Time series of (a) solar wind speed, (b) solar wind proton density, (c) IMF Bz, (d) IMF By, (e) SYM-H and (f) AL index on March 1–7, 2017. The event time of focus in this study is highlighted by magenta lines (at 2–3 UT on March 7).

within the riometer FOVs of IVA and SOD of Figure 4a. At 2:37 UT, a bright patch appeared above SOD, and then in a few minutes, pulsating auroral activities expanded equatorward, increasing the emission intensity. While this study made a comparison with the CNA by separating measurements at 2:40 UT, the same analyses were also performed by altering the separation time every minute from 2:35 to 2:39 UT. However, there was no notable difference in the conclusion.

3.2. CNA Variations With the Low-Pass Component

According to a study of pulsating aurora by Yamamoto (1988), oscillation periods of the main pulsation in the pulsating aurora may be shorter than 40 s. Then, in this study, we define the auroral intensity variations characterized by oscillation periods shorter than 40 s as being attributed to the pulsating aurora and describe
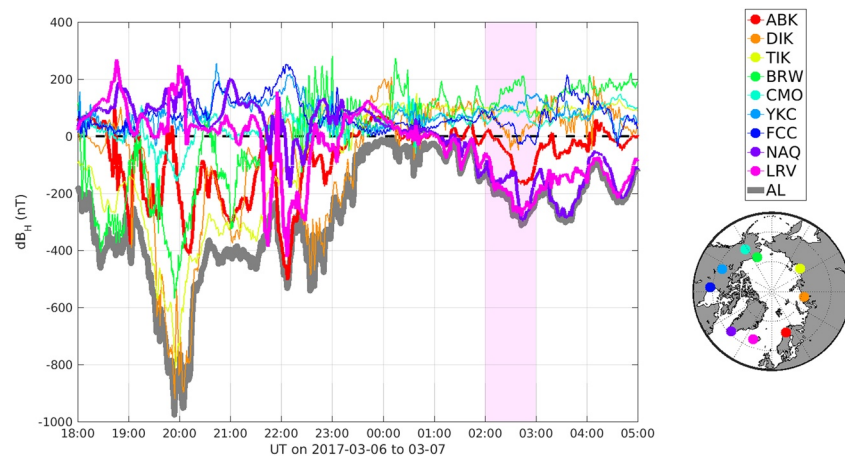
Figure 3. Temporal variations in the magnetometer measurement (H component) at 9 AL stations (in color; ABK: Abisko, DIK: Dixon, TIK: Tixie, BRW: Barrow, CMO: College, YKC: Yellowknife, FCC: Fort Churchill, NAQ: Narssarssuaq, and LRV: Leirvogur) and the OMNI AL index (gray) from 18 to 5 UT on March 6–7, 2017. The event time (2–3 UT on March 7, 2017) is hatched in magenta. The locations of the AL stations are marked in the map.

them as high-pass components. In contrast, variations with periods longer than 40 s are described as low-pass components. The first and second panels from the top of Figure 5 show temporal variations in the CNA and the camera image count, respectively, from 2:00 to 3:00 UT at IVA (Figures 5a and 5b), SOD (Figures 5e and 5f), and ROV (Figures 5i and 5j). For the second half of the selected time interval (i.e., approximately after 2:30 UT), the sky was illuminated by twilight, which aggravated the contamination level when extracting the auroral intensity. To minimize the effects of the twilight, quiet-time measurements from the same camera at the same time interval but on March 8, 2018 (that is, in one year; also clear sky) were subtracted to create Figures 5b, 5f and 5j. The camera image count (thin curves in Figures 5b, 5f and 5j) was derived by computing the average of measurements within individual riometer FOVs but weighting the horizontal pattern of the sensitivity shown in Figure 1b. The low-pass component (thick curve) is derived by the 40-s running mean as defined above. The results in the lower two panels will be discussed later in regard to the pulsating aurora effects.

The left column of Figure 6 shows the relationships between CNA and the spatially averaged camera count of the low-pass components at the three riometer sites. The square root of the mean camera count has been plotted because CNA in dB is expected to be proportional to it according to Equation 4. Measurements for T1 and T2 are marked in blue and orange, respectively. The regression line for each interval is drawn in corresponding colors, and the correlation coefficient is presented in parentheses. To match the time resolution between the CNA and the camera count, a 1-min mean camera count was calculated in advance, so the numbers of data points were 40 and 20 for T1 and T2, respectively, at all sites. In terms of the low-pass component at IVA, the correlation coefficients are relatively low (0.28 and 0.33). At SOD and ROV, the relationship appears to be more clearly characterized by linearity, as theoretically expected. Of particular interest is the change in the inclination at SOD and ROV, which increases turning from T1 to T2 or appearing brighter patches in the greater part of the camera FOV. This trend can also be vaguely identified at IVA. The increase in the inclination with time shift from T1 to T2 will be discussed in Section 4.2.

### 3.3. CNA Variations With the High-Pass Component

The high-pass component of the camera image count was derived by subtracting the 40-s running mean from the 0.1 s mean, that is, the residual between values in thin and thick curves shown in Figures 5b, 5f and 5j at IVA, SOD and ROV, respectively. The high-pass component at each site is shown in Figures 5c, 5g and 5k. The fast Fourier transform (FFT) was applied to the results with a time window of 51.2 s, which corresponds to 512 data points. Figures 5d, 5h and 5l show values of the FFT spectrum power integrated in the frequency domain from 0.025 to 1 Hz (i.e., 1–40 s in the oscillation period domain). The unit is count. The values were interpolated to match the 1-min time resolution of CNA.
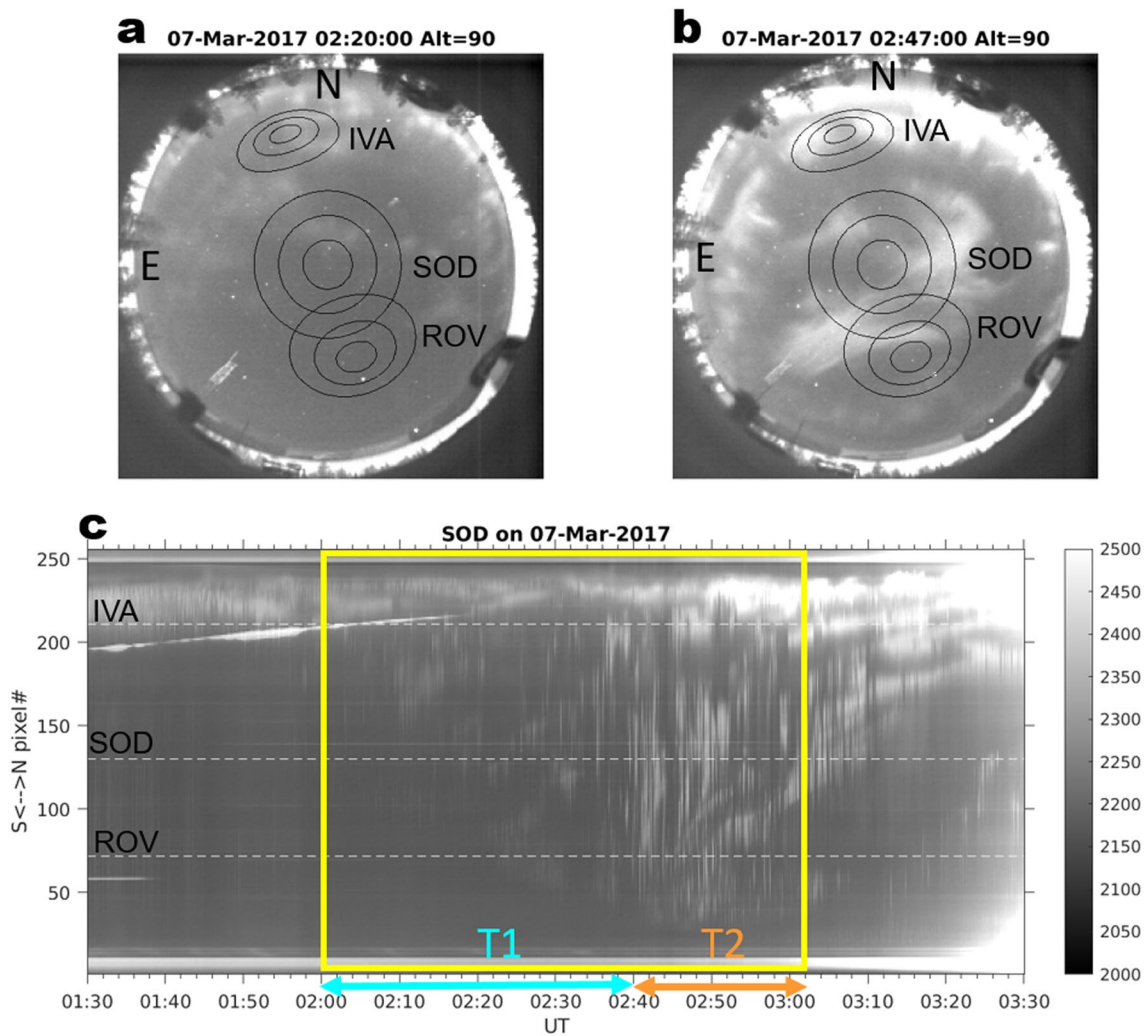
Figure 4. (a and b) All-sky images taken with the Sodankylä electron multiplying charge-coupled device camera at 02:20:00 and 02:47:00 UT on March 7, 2017. The top and left of each image are north and east, respectively. The riometer sensitivity pattern shown in Figure 1b are overlaid on the images at elevation angles of 60°, 70°, and 80°, assuming the riometer sensitivity peak at 90 km. (c) Keogram made of the electron multiplying charge-coupled device camera images from 01:30 to 03:30 UT on March 7, 2017. The time interval of focus in this study is highlighted by a yellow box. The light blue and orange arrows represent time intervals T1 and T2 (see text in detail). Three horizontal dashed lines are marked at pixels corresponding to latitudes of Ivalo, Sodankylä, and Rovaniemi.

The right column of Figure 6 shows the relationships between CNA and the mean FFT power of the high-pass component at the three riometer sites. The figure format is the same as the left column for the low-pass component. The relationship at IVA (Figure 6d) has a low correlation at T2, probably because of mixture of pulsating and nonpulsating auroral activities in the riometer FOV (see Figure 4c). In contrast, the results at SOD and ROV (Figures 6e and 6f, respectively) had a higher correlation than those at IVA. In the case of SOD, there was hardly any change in the inclination of the regression line between T1 and T2. In contrast, in the case of ROV, the inclination decreased with turning from T1 to T2. This study focuses on the inclination change with time shift from T1 to T2, and the inclination change may be attributed to an energy shift of precipitating electrons, as elucidated in Section 4.1.
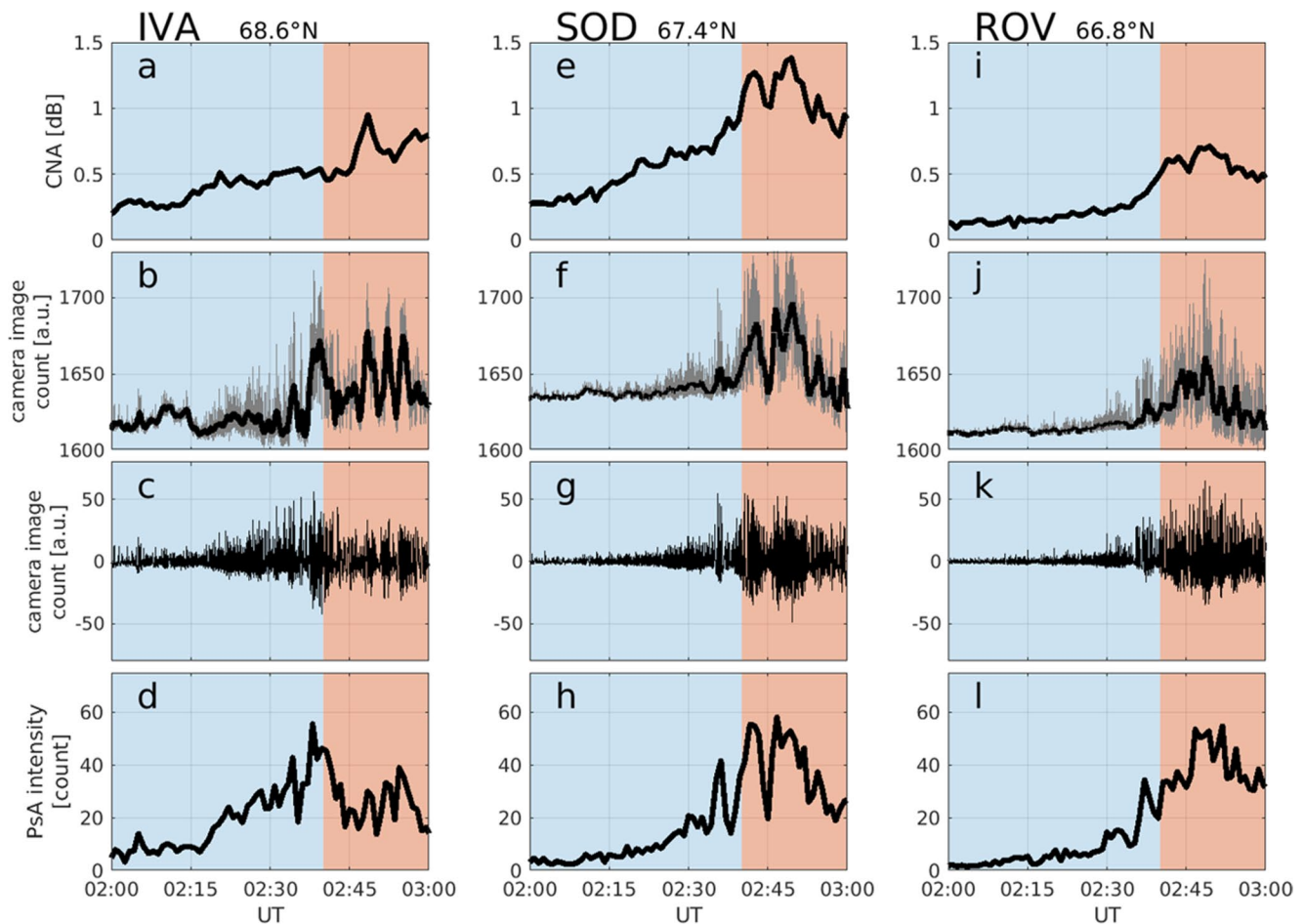
Figure 5. Temporal variations in (a, e, and i) CNA, (b, f, and j) camera image count of 0.1 s time resolution and the 40-s running mean (thin and thick, respectively), (c, g, and k) difference between 0.1 and 40 s mean camera image counts and (d, h, and l) integrated fast Fourier transform (FFT) power in the frequency direction from 0.025 to 1 Hz at each site (Ivalo, Sodankylä, and Rovaniemi from left to right). Time intervals T1 and T2 are hatched in blue and orange, respectively.

4. Discussion

This study analyzed the camera image count and the riometer-measured CNA in the morning sector of Scandinavia at 2–3 UT (approximately 5 MLT) but during the third substorm at the night of March 7, 2017. The substorm onset occurred westward of Scandinavia. Separating the 1-h interval into two segments, T1 and T2 (before and after 2:40 UT, respectively), proportionality relating the auroral brightness to the CNA was estimated at three latitudes from 66.8° to 68.6°N, which had different features dependent on the two time segments and latitudes. Of particular interest is dependency on the auroral oscillating periods, shorter than 40 s, corresponding to the main pulsation of the pulsating aurora, or longer than it. According to a general vertical gap between representative altitudes of aurora and CNA, variations in the proportionality should be related to changes in the precipitating energy spectrum. Sections 4.1 and 4.2 discuss temporal evolutions in the precipitating energy spectrum for the high and low pass components, respectively.

4.1. Precipitating Electron Spectrum: High-Pass Component

The relationship between CNA and the high-pass component of the camera image count was investigated by grouping measurements based on aurora morphological change, as presented in Section 3.3. This relationship revealed shifts in the inclination from T1 to T2 that were dependent on the riometer location or latitude, as shown in the right column of Figure 6. Since the correlation coefficients at IVA for T2 are
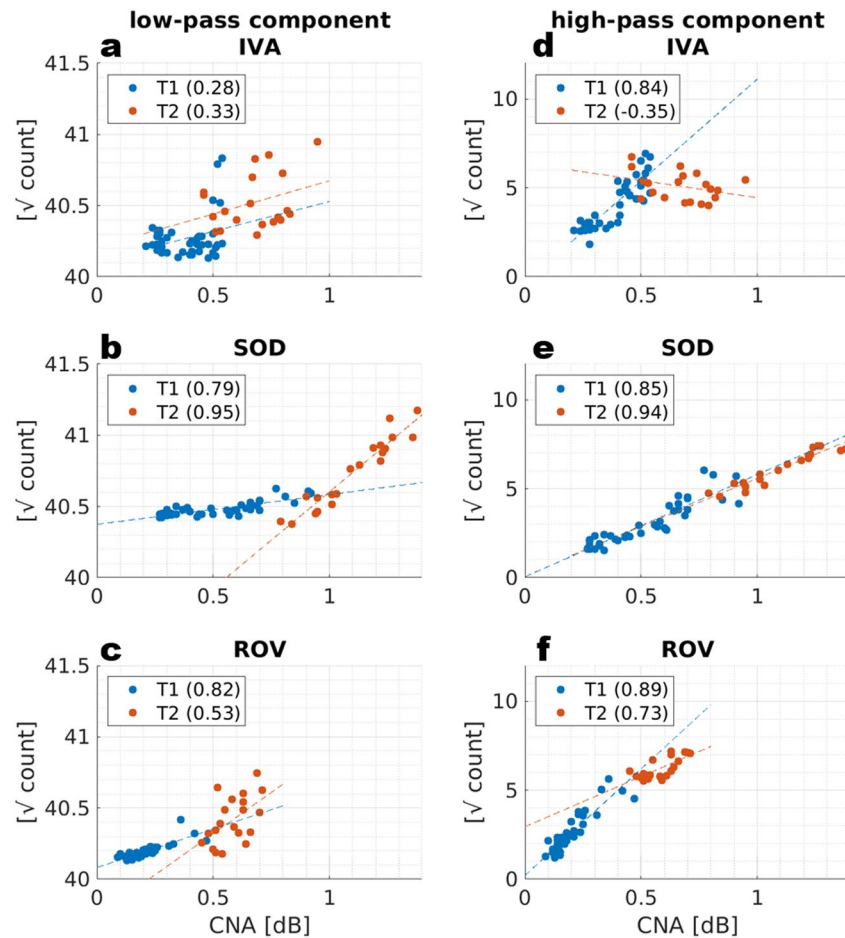
Figure 6. Scatter plot of cosmic noise absorption versus square root of the camera image count at Ivalo, Sodankylä, and Rovaniemi (from top to bottom) for time periods of T1 (blue) and T2 (orange). The left and right panels present the results for the low- and high-pass components, respectively (see text in detail). The dashed line is the regression line at each interval. The correlation coefficient is presented in parentheses.

considerably low, even a negative value, this section will focus on the results at SOD and ROV, which are presented in Figures 6e and 6f, respectively.

The most remarkable difference between the two results can be seen in the inclination of the regression line, which shows nearly stable linearity at SOD for T1 and T2, but at ROV, it becomes a flatter slope at T2 than T1. Altitudinal gaps between the auroral emission height and the CNA sensitivity peak of 90 km may be a key issue to understand this feature. As mentioned in Section 1, in the morning time sector, both the optical emission height and E-region density peak height tend to decline with time but retain an altitudinal gap of approximately 10 km, keeping higher altitude of the optical emission peak than that of the density peak (Hosokawa & Ogawa, 2015; Partamies et al., 2017). These declinations suggest increase in the mean precipitating electron energy, that is, hardening of the precipitating electron spectrum. During the pulsating aurora, spectrum hardening has been measured above 10 keV with the rocket and the incoherent scatter radar (Oyama et al., 2017; Sandahl et al., 1980). It is assumed that height of the pulsating auroral optical emission (e.g., Kataoka et al., 2013) is higher than that of the riometer measurement; in other words, the pulsating auroral emission intensity and CNA represent the flux of lower- and higher-energy electron precipitation, respectively.

Figures 7a and 7b demonstrate spectrum changes from T1 to T2 at SOD and ROV, respectively, or at lower and higher latitudes of the pulsating auroral appearance in this event. E_{opt} and E_{CNA} are precipitating electron energies represented by auroral and CNA measurements, respectively. As mentioned before, these
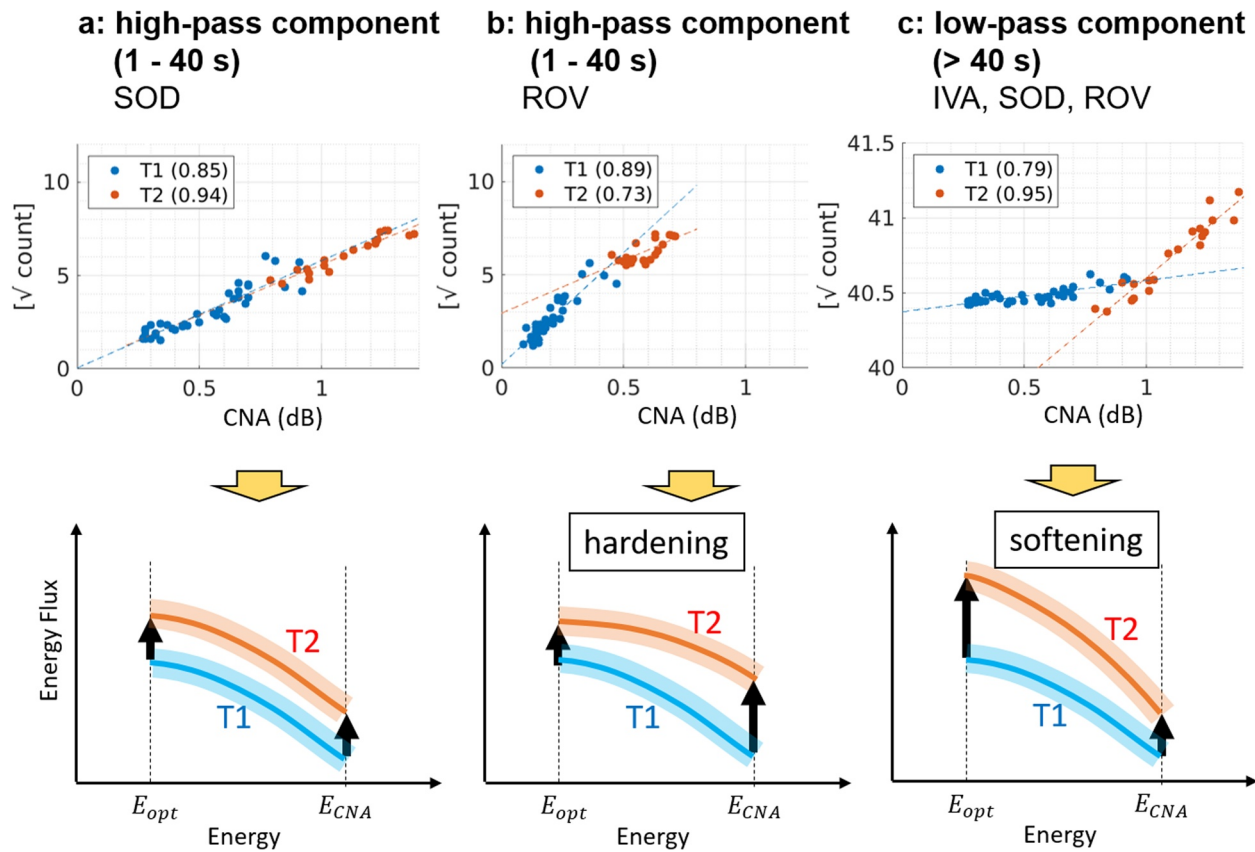
Figure 7. Schematic drawing showing the temporal change in the energy flux spectrum from T1 (blue) to T2 (orange), which were estimated from the interrelation between the cosmic noise absorption and the auroral brightness (top panels) for the high-pass component at (a) Sodankylä and (b) Rovaniemi and for (c) the low-pass component at the three sites. Transparent hatches overlaid on the spectrum are responsible for variations for T1 (blue) and T2 (orange).

energies may be 10 and 40 keV, respectively. It is assumed that the precipitating electron flux decreases with energy from 10 to 40 keV (see Figures 7 and 8 of Oyama et al., 2017). In the case of SOD (Figure 7a), the inclination of the interrelation between CNA and the auroral intensity remained uniform throughout the event time. This finding suggests that variations in the precipitating electron fluxes at E_{opt} and E_{CNA} have retained the flux ratio between the two energy levels, and Figure 7a illustrates the synchronized flux increase at SOD from T1 to T2. In the case of ROV, Figure 7b shows that precipitating electrons for T2 more effectively contributed to a CNA increase than those at T1. This suggests hardening of the precipitation spectrum from T1 to T2.

Comparing results at SOD (Figure 7a) and ROV (Figure 7b), it revealed that the precipitating electron spectrum hardened at the lower latitudinal side of the pulsating aurora and its patch development, that is, ROV. This result is consistent with previous observations using the EISCAT radar, the Kilpisjärvi Atmospheric Imaging Receiver Array (KAIRA) and cameras in northern Scandinavia (Oyama et al., 2017), which showed that the energy of the precipitating electron increased with auroral patch formation at the equator side of the auroral oval. On the other hand, in this study, there was no clear visible difference in the auroral patch pattern between the two riometer FOVs of the SOD and ROV. This finding implies that the appearance of the patch can be used as a proxy for hardening of the precipitating electron spectrum, but the spectrum may not be uniform in the patch area.

4.2. Precipitating Electron Spectrum: Low-Pass Component

Upper panel of Figure 7c shows that the inclination of the CNA-vs-camera count linearity increases from T1 to T2 for the case of the low-pass component. Applying the concept based on the altitudinal gap between the auroral emission height and the CNA sensitivity peak, which was described in Section 4.1, the inclination
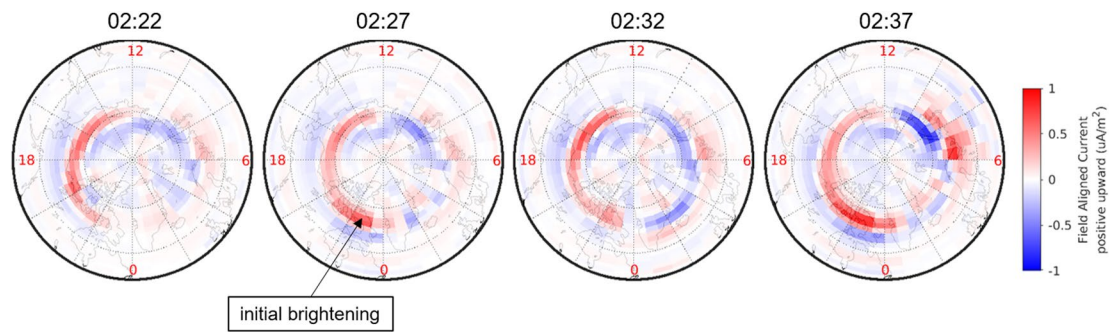
Figure 8. Field-aligned current density patterns at the ionospheric height (positive upward) from 02:22 to 02:37 UT on March 7, 2017. Additional lines of latitude and longitude are drawn every 15°. Magnetic local times are marked in red.

increase suggests softening of the precipitating electron spectrum with time shift from T1 to T2, and lower panel of Figure 7c illustrates the spectrum change from T1 to T2. This finding for the low-pass component is a notable distinction from the estimated spectrum for high-pass component. While auroral brightening results from an increase in the precipitating electron flux, the amount of the flux increase is dependent on auroral intensity modulation and latitude according to the results in this study.

However, we may require further spectral analyses for the low-pass component. The analysis in this study was performed by separating the optical data into low- and high-pass components, as defined in Section 3.2. The high-pass component approximately represents the variations associated with the pulsating aurora, as shown in Figures 5c, 5g and 5k. The low-pass component (thick curves in Figures 5b, 5f and 5j) appears to vary following the amplitude of the high-pass component. Positive deviations in the high-pass component (Figures 5c, 5g and 5k) are larger than negative deviations through the selected time interval because the pulsating OFF interval can be longer than the ON interval (Yamamoto, 1988), and the low-pass component tends to have lower values off the center between the ON and OFF peaks. Since the high-pass component has been defined as a deviation from the low-pass component, the off center value results in larger positive deviations of the high-pass component. As a result, the low-pass component is also affected by trends in the auroral activity that are longer than 40 s; thus, it is reasonable to assume that the low-pass component is affected by both nonpulsating and pulsating auroral variations, which may prove to be an ambiguous issue.

4.3. Auroral Development in the Morning Sector at Substorm Onset

The event in this study was found in the third substorm of the night as described in Section 3.1. The AL index and measurements at nine AL stations shown in Figure 3 imply that the substorm-related ionospheric current was principally developed in the Greenland/Iceland area. However, this estimate may not be accurate because of spatially discrete measurements, as presented in the map in Figure 3. Then, the field-aligned current (FAC) pattern at the ionospheric height was calculated with the Assimilative Mapping of Geospace Observations (AMGeO) (AMGeO Collaboration, 2019; Matsuo et al., 2015; Shi et al., 2020a, 2020b) to find the location of the initial brightening. Figure 8 presents four FAC patterns from 02:22 to 02:37 UT on March 7, 2017. The positive (negative) value drawn with a reddish (bluish) hue is the upward (downward) FAC, respectively. Scandinavia is located in the morning sector (approximately 5 MLT), and the west coast of Greenland is located at midnight in these UTs. For the selected 15 min, clear Region 1 (R1) and Region 2 (R2) FAC patterns can be seen with fluctuations in magnitude. Of particular interest is a regional increase in the R1 upward FAC at 02:27 UT in northern North America, which is evidence of the initial brightening of the third substorm. This area was not covered by the AL magnetometer measurements (see the map of Figure 3), which might be a reason for the unclear development of the negative bay related to the third substorm. In the first three FAC patterns, there is almost no change in the Scandinavia region, which is consistent with moderately stable auroral brightness and morphology, as presented in Figure 4c. However, at 02:37 UT, R1 and R2 FACs were obviously enhanced from Scandinavia to middle Siberia, coinciding with an increase in northern North America. The time of these enhancements concurs with that of the equatorward development of the aurora that appeared in northern Scandinavia (see Figure 4c). This finding suggests that the formation of the equatorward development of the pulsating aurora is associated with FAC

intensification in the morning sector. Synchronization with the FAC enhancement before midnight is also an attractive point in terms of a possible midnight-morning link in the magnetosphere, but this is beyond the scope of this work and is left for future work.

Since primary development of the third substorm was centered in northern North America, measurements in Finland were made on the east side of magnetic midnight or in the morning sector. A shift from T1 to T2 occurred at the AL minimum, and T1 and T2 can be a part of the substorm expansion and recovery phases, respectively. The temporal evolution of the auroral morphology for T1 and T2 is different from that typically seen in the two phases around the midnight substorm region (Akasofu, 1964). As seen in the keogram (Figure 4c), pulsating auroral patches appeared at the equator side of the auroral oval at early T1 but poleward to the SOD. Coinciding with the AL minimum, pulsating auroral patches expanded more equatorward, increasing the brightness. While pulsating aurorae may be seen at the substorm expansion phase, the pulsating aurora interval statistically starts at the end of the expansion phase or at the early recovery phase (Partamies et al., 2017). Thus, the development of the pulsating aurora in the morning sector may rely on different progress from that near magnetic midnight. As coordinating measurements with high-speed cameras on the ground and magnetospheric satellites recently showed, enhancements of the whistler mode waves in the magnetosphere agree with pulsation of auroral brightness (Hosokawa et al., 2020; Kasahara et al., 2018). This finding is conspicuous experimental evidence demonstrating the interactions outside the plasmapause at the magnetic equator between energetic electrons and whistler mode chorus waves in generating the pulsating aurora, as wave-particle interactions (WPIs) are believed to be the generation mechanism (Miyoshi, Saito, et al., 2015). Equatorward development of the pulsating auroral patch should be associated with inward penetration of the modulation region of WPI in the magnetospheric equator. Magnetospheric features during the equatorward evolution of the pulsating auroral patch will be an important target to investigate in future work.

5. Summary and Conclusions

This study analyzed data from a high-speed auroral camera and three riometers in Finland (from high to low latitudes, Ivalo, Sodankylä and Rovaniemi) during a pulsating aurora and investigated the relationships between the emission intensity and CNA. The event was found in the morning (2–3 UT or 4.5–5.5 MLT) during the third substorm on March 7, 2017 at the recovery phase of the CIR-induced storm. After a short time (approximately 10 min) from the substorm onset, pulsating auroral patches expanded equatorward with increasing brightness. Based on a comparison between the camera image count and CNA, we estimated changes in the precipitating electron spectrum before and after the equatorward expansion. This estimation was made at the three riometer latitudes separating the optical data into two frequency components (oscillation frequencies lower and higher than 0.025 Hz, corresponding to a 40 s oscillation period). An analysis of the high-pass component suggested hardening of the precipitating electron spectrum at Rovaniemi, which is the lower latitudinal side of the pulsating auroral area but hardening did not occur at Sodankylä, which is the higher latitudinal side. An analysis of the low-pass component suggested softening of the spectrum at all three latitudes. This event study speculates that the appearance of the pulsating auroral patch is a visible sign of hardening of the precipitating electron spectrum, which is consistent with the results of Oyama et al. (2017). However, softening of the spectrum and dependencies on the emission intensity frequency and latitude have not been reported to the best of our knowledge. To understand causality to produce spectrum hardening/softening and auroral patches, we need more studies on WPI and auroral morphological changes analyzing conjunction data with magnetospheric satellites and ground-based cameras.

Data Availability Statement

The data files were obtained from the ERG-Science Center operated by ISAS/JAXA and ISEE/Nagoya University (http://ergsc.isee.nagoya-u.ac.jp/index.shtml.en). The SGO riometer quick look plots can be viewed at http://www.sgo.fi/Data/Riometer/rioData.php, and the data are available upon request.

References

Akasofu, S.-I. (1964). The development of the auroral substorm, Planet. *Space Sci*, *12*, 273–282. https://doi.org/10.1016/0032-0633(64)90151-5

AMGeO Collaboration. (2019). *A collaborative data science platform for the Geospace community: Assimilative mapping of Geospace observations (AMGeO) v1*. Zenodo. https://doi.org/10.5281/zenodo.3564914

Arnoldy, R. L., Dragoon, K., Cahill, L. J., Mende, S. B., & Rosenberg, T. J. (1982). Detailed correlations of magnetic field and riometer observations at L = 4.2 with pulsating aurora. *Journal of Geophysical Research*, *87*(A12), 10449. https://doi.org/10.1029/JA087iA12p10449

Brekke, A. (1971). On the correlation between pulsating aurora and cosmic radio noise absorption. *Planetary and Space Science*, *19*, 891–896. https://doi.org/10.1016/0032-0633(71)90140-1

Campbell, W. H., & Leinbach, H. (1961). Ionospheric absorption at times of auroral and magnetic pulsations. *Journal of Geophysical Research*, *66*, 25–34. https://doi.org/10.1029/JZ066i001p00025

D'Angelo, N. (1976). On riometers. *Journal of Geophysical Research*, *81*(31), 5581–5582. https://doi.org/10.1029/JA081i031p05581

Grandin, M., Kero, A., Partamies, N., McKay, D., Whiter, D., Kozlovsky, A., & Miyoshi, Y. (2017). Observation of pulsating aurora signatures in cosmic noise absorption data. *Geophysical Research Letters*, *44*, 5292–5300. https://doi.org/10.1002/2017GL073901

Grono, E., & Donovan, E. (2018). Differentiating diffuse auroras based on phenomenology. *Annales Geophysicae*, *36*, 891–898. https://doi.org/10.5194/angeo-36-891-2018

Hargreaves, J. K. (1995). *The solar-terrestrial environment*. Cambridge University Press.

Hashimoto, A., Shiokawa, K., Otsuka, Y., Oyama, S.-I., Nozawa, S., Hori, T., et al. (2015). Statistical study of auroral fragmentation into patches. *Journal of Geophysical Research: Space Physics*, *120*, 6207–6217. https://doi.org/10.1002/2015JA021000

Hosokawa, K., & Ogawa, Y. (2015). Ionospheric variation during pulsating aurora. *Journal of Geophysical Research: Space Physics*, *120*, 5943–5957. https://doi.org/10.1002/2015JA021401

Hosokawa, K., Oyama, S. I., Ogawa, Y., Miyoshi, Y., Kurita, S., & Teramoto, M. (2020). A ground-based instrument suite for integrated high-time resolution measurements of pulsating aurora with Arase. *Journal of Geophysical Research*. Retrieved from https://www.essoar.org/doi/10.1002/essoar.10504721.1

Jussila, J. R. T., Aikio, A. T., Shalimov, S., & Marple, S. R. (2004). Cosmic radio noise absorption events associated with equatorward drifting arcs during a substorm growth phase. *Annales Geophysicae*, *22*, 1675–1686. https://doi.org/10.5194/angeo-22-1675-2004

Kasahara, S., Miyoshi, Y., Yokota, S., Mitani, T., Kasahara, Y., Matsuda, S., et al. (2018). Pulsating aurora from electron scattering by chorus waves. *Nature*, *554*, 337–340. https://doi.org/10.1038/nature25505

Kataoka, R., & Miyoshi, Y. (2006). Flux enhancement of radiation belt electrons during geomagnetic storms driven by coronal mass ejections and corotating interaction regions. *Space Weather*, *4*, S09004. https://doi.org/10.1029/2005SW000211

Kataoka, R., Miyoshi, Y., Shigematsu, K., Hampton, D., Mori, Y., Kubo, T., et al. (2013). Stereoscopic determination of all-sky altitude map of aurora using two ground-based Nikon DSLR cameras. *Annales Geophysicae*, *31*, 1543–1548. https://doi.org/10.5194/angeo-31-1543-2013

Matsuo, T., Knipp, D. J., Richmond, A. D., Kilcommons, L., & Anderson, B. J. (2015). Inverse procedure for high-latitude ionospheric electrodynamics: Analysis of satellite-borne magnetometer data. *Journal of Geophysical Research: Space Physics*, *120*, 5241–5251. https://doi.org/10.1002/2014JA020565

McKay, D., Partamies, N., & Vierinen, J. (2018). Pulsating aurora and cosmic noise absorption associated with growth-phase arcs, *Annales Geophysicae*, *36*, 59–69. https://doi.org/10.5194/angeo-36-59-2018

Miyoshi, Y., Kataoka, R., Kasahara, Y., Kumamoto, A., Nagai, T., & Thomsen, M. F. (2013). High-speed solar wind with southward interplanetary magnetic field causes relativistic electron flux enhancement of the outer radiation belt via enhanced condition of whistler waves. *Geophysical Research Letters*, *40*, 4520–4525. https://doi.org/10.1002/grl.50916

Miyoshi, Y., Oyama, S., Saito, S., Kurita, S., Fujiwara, H., Kataoka, R., et al. (2015). Energetic electron precipitation associated with pulsating aurora: EISCAT and Van Allen Probes observations. *Journal of Geophysical Research: Space Physics*, *120*, 2754–2766. https://doi.org/10.1002/2014JA020690

Miyoshi, Y., Saito, S., Seki, K., Nishiyama, T., Kataoka, R., Asamura, K., et al. (2015). Relation between fine structure of energy spectra for pulsating aurora electrons and frequency spectra of whistler mode chorus waves. *Journal of Geophysical Research: Space Physics*, *120*, 7728–7736. https://doi.org/10.1002/2015JA021562

Ni, B., Thorne, R. M., Meredith, N. P., Horne, R. B., & Shprits, Y. Y. (2011). Resonant scattering of plasma sheet electrons leading to diffuse auroral precipitation: 2. Evaluation for whistler mode chorus waves. *Journal of Geophysical Research*, *116*, A04219. https://doi.org/10.1029/2010JA016233

Oyama, S., Kero, A., Rodger, C. J., Clilverd, M. A., Miyoshi, Y., Partamies, N., et al. (2017). Energetic electron precipitation and auroral morphology at the substorm recovery phase. *Journal of Geophysical Research: Space Physics*, *122*, 6508–6527. https://doi.org/10.1002/2016JA023484

Oyama, S., Watanabe, T., Fujii, R., Nozawa, S., & Tsuda, T. T. (2013). Layered conductance in the ionosphere estimated using data from a multiwavelength photometer at the European Incoherent Scatter radar site. *Antarctic Record*, *57*(3), 339–356.

Ozaki, M., Miyoshi, Y., Shiokawa, K., Hosokawa, K., Oyama, S. I., Kataoka, R., et al. (2019). Visualization of rapid electron precipitation via chorus element wave–particle interactions. *Nature Communication*, *10*, 257. https://doi.org/10.1038/s41467-018-07996-z

Partamies, N., Whiter, D., Kadokura, A., Kauristie, K., Nesse Tyssøy, H., Massetti, S., et al. (2017). Occurrence and average behavior of pulsating aurora. *Journal of Geophysical Research: Space Physics*, *122*, 5606–5618. https://doi.org/10.1002/2017JA024039

Sandahl, I., Eliasson, L., & Lundin, R. (1980). Rocket observations of precipitating electrons over a pulsating aurora. *Geophysical Research Letters*, *7*, 309–312. https://doi.org/10.1029/GL007i005p00309

Shi, Y., Knipp, D. J., Matsuo, T., Kilcommons, L., & Anderson, B. (2020a). Event studies of high-latitude FACs with inverse and assimilative analysis of AMPERE magnetometer data. *Journal of Geophysical Research: Space Physics*, *125*, e2019JA027266. https://doi.org/10.1029/2019JA027266

Shi, Y., Knipp, D. J., Matsuo, T., Kilcommons, L., & Anderson, B. (2020b). Modes of (FACs) variability and their hemispheric asymmetry revealed by inverse and assimilative analysis of iridium magnetometer data. *Journal of Geophysical Research: Space Physics*, *125*, e2019JA027265. https://doi.org/10.1029/2019JA027265

Shiokawa, K., Hashimoto, A., Hori, T., Sakaguchi, K., Ogawa, Y., Donovan, E., et al. (2014). Auroral fragmentation into patches. *Journal of Geophysical Research: Space Physics*, *119*, 8249–8261. https://doi.org/10.1002/2014JA020050

Stauning, P. (1984). Absorption of cosmic noise in the E-region during electron heating events. A new class of riometer absorption events. *Geophysical Research Letters*, *11*, 1184–1187. https://doi.org/10.1029/GL011i012p01184

Tanaka, Y., Ishii, M., Kubota, M., Murayama, Y., Mori, H., & Lummerzheim, D. (2007). Cosmic noise absorption observed with imaging riometer in Alaska: Use of CNA to estimate energy spectra of auroral precipitating electrons. *Journal of the National Institute of Information and Communications Technology*, *54*, 97–105.

Tesema, F., Partamies, N., Nesse Tyssøy, H., & McKay, D. (2020). Observations of precipitation energies during different types of pulsating aurora. *Annales Geophysicae*, *38*, 1191–1202. https://doi.org/10.5194/angeo-38-1191-2020

Thorne, R. M., Ni, B., Tao, X., Horne, R. B., & Meredith, N. P. (2010). Scattering by chorus waves as the dominant cause of diffuse auroral precipitation. *Nature*, *467*, 943–946. https://doi.org/10.1038/nature09467

Torr, D. G., Torr, M. R., Walker, J. C. G., Brace, L. H., Brinton, H. C., Hanson, W. B., et al. (1976). Recombination of NO+ in the ionosphere. *Geophysical Research Letters*, *3*(4), 209–212. https://doi.org/10.1029/GL003i004p00209

Turunen, E., Verronen, P. T., Seppälä, A., Rodger, C. J., Clilverd, M. A., Tamminen, J., et al. (2009). Impact of different precipitation energies on NOx generation during geomagnetic storms. *Journal of Atmospheric and Solar-Terrestrial Physics*, *71*, 1176–1189. https://doi.org/10.1016/j.jastp.2008.07.005

Vickrey, J. F., Vondrak, R. R., & Matthews, S. J. (1982). Energy deposition by precipitating particles and Joule dissipation in the auroral ionosphere. *Journal of Geophysical Research*, *87*(A7), 5184–5196. https://doi.org/10.1029/JA087iA07p05184

Yamamoto, T. (1988). On the temporal fluctuations of pulsating auroral luminosity. *Journal of Geophysical Research*, *93*(A2), 897–911. https://doi.org/10.1029/JA093iA02p00897

Yang, B., Spanswick, E., Liang, J., Grono, E., & Donovan, E. (2019). Responses of different types of pulsating aurora in cosmic noise absorption. *Geophysical Research Letters*, *46*, 5717–5724. https://doi.org/10.1029/2019GL083289